Available online at www.sciencedirect.com

jmr&t Journal of Materials Research and Technology

www.jmrt.com.br

Original Article

Physical simulation as a tool to understand friction stir processed X80 pipeline steel plate complex microstructures

Julian Avila[a,*], *Julian Escobar*[b], *Barbara Cunha*[b], *William Magalhães*[b], *Paulo Mei*[b], *Johnnatan Rodriguez*[c], *Haroldo Pinto*[d], *Antonio Ramirez*[e]

[a] *UNESP – São Paulo State University, Campus of São João da Boa Vista, Av. Prof*[a] *Isette Corrêa Fontão, 505, Jardim das Flores, 13876-750 São João da Boa Vista, SP, Brazil*

[b] *School of Mechanical Engineering, University of Campinas, Rua Mendeleyev 200, Campinas, SP 13083860, Brazil*

[c] *Department of Mechanical Engineering, EIA University, Envigado, Antioquia, Colombia*

[d] *University of São Paulo (USP) at São Carlos School of Engineering, Av. João Dagnone, 1100, Jd. Sta Angelina, São Carlos, SP 13563120, Brazil*

[e] *The Ohio State University, 1248 Arthur E. Adams Drive, Columbus, OH 43221, USA*

ARTICLE INFO

Article history:
Received 6 May 2018
Accepted 26 September 2018
Available online 17 November 2018

Keywords:
Friction stir processing
Heat-affected zone
X80 pipeline steel
Bainite
Continuous cooling transformation

ABSTRACT

The thermal cycles associated to friction stir welding and processing produce a wide range of microstructures, resulting in different mechanical behaviors along the weld. Most research efforts have focused on the development of welding parameters to obtain sound welds, yet there is still an opportunity for performance improvement based on the understanding of how microstructures are produced. This work explored the different microstructures obtained after physical simulation of an X80 pipeline steel, as a function of the cooling rate and the isothermal transformation temperature. The aim was to study the development of complex mixed microstructures under controlled conditions, in order to compare them to the ones obtained after friction stir processing. As result of the continuous cooling and isothermal thermal simulations, intermediated and high cooling rates, the microstructures matched with those found at the processed plates. These results might help developing a better cooling control after welding.

1. Introduction

Friction stir welding (FSW) is an alternative joining processes in solid state. The peak temperatures obtained during FSW of high strength low alloy (HSLA) are considerably lower than those from arc welding [1]. Thus, the microstructures obtained after FSW are expected to be different from those

* *Corresponding author.*
E-mail: julian.avila@unesp.br (J. Avila).

https://doi.org/10.1016/j.jmrt.2018.09.009

after arc welding. First, no solidification microstructures, i.e., fusion zone and partially melted heat-affected zone, are found after FSW. The Coarse-grained heat-affected zone (CGHAZ), observed after arc welding, evidence typical grain sizes between 75 and 150 μm [2]. In fact, such CGHAZ has been divided into two sub zones: the coarser CGHAZ (near the fusion line) and the finer-grained HAZ (away from the fusion line) [3]. The former is not observed in FSW; while the latter is equivalent to the stir zone (SZ) in terms of grain size, hardness, toughness [3], and bainitic microstructure [4]. Nevertheless, after FSW, the CGHAZ has been considered absent [3] or not detected [4] by conventional light optical microscopy (LOM) or scanning electron microscopy (SEM), because the obtained grain size is very similar to the one at the base material. A thermo-mechanically affected zone (TMAZ) is observed right beside the SZ, followed by the fine grain heat affected zone (FGHAZ), the inter-critical heat-affected zone (ICHAZ) and the sub-critical heat-affected zone (SCHAZ). After FSW, the grain size along the HAZ, measured with electron backscattering diffraction (EBSD), has shown very small variations of around 1 μm [4]. However, subzones within the HAZ after FSW/P can be found using a combination of hardness and EBSD mapping [5,6].

The X80 HSLA steel is fabricated by a thermomechanical controlled processes (TMCP) followed by accelerated cooling (ACC), which controls the austenite to ferrite transformation, providing high strength, high toughness and good weldability [7]. The microstructure of HSLA steels is a matrix composed by ferrite and bainite [8]. Depending on the nominal carbon content and the cooling rate, different so-called secondary phases (SP) and constituents, such as martensite-austenite (MA), degenerated pearlite (DP), bainite (B) and martensite (M) [9] can appear. After FSW, the microstructure is affected by several factors, such as the strain and temperature [4,10] during the metal stirring and the subsequent cooling rates [11–13]. Previous works published elsewhere have clearly shown that the as-processed microstructure of X80 pipeline steels can be rather complex due to the mixing of polygonal ferrite (PF), quasi-polygonal ferrite (QPF), acicular ferrite (AF), granular bainite (GB), bainite with irregular plates (B-IP), bainite with straight plates (B-SP) and fine secondary phases [6]. Furthermore, an additional microstructural gradient is found at the hard zone (HZ) inside the SZ, which has been reported to undergo the highest strains and temperatures of the whole weld [12,14]. Therefore, different peak temperatures and cooling rates can be obtained along the stir zone because of such thermomechanical inhomogeneities [15], resulting in the complex mixing of hard phases [5,6,15].

This work encompasses an experimental effort to obtain, under controlled conditions, mixed and isolated microstructures, through continuous cooling (CCT) and time temperature (TTT) transformation experiments, respectively, using physical simulation. This can be very useful to isolate or maximize the presence of a phase of interest, and to associate such microstructure to the resulting hardness. The results were compared to the as-processed microstructure after FSP of an X80 pipeline steel plate. The microstructural comparison was performed by LOM, SEM and microhardness tests.

Table 1 – Chemical composition of the API 5L X80 pipeline steel.

C	Si	Mn	Mo	Nb	Ni	Ti	V	Fe
0.04	0.32	1.56	0.19	0.03	0.24	0.01	0.01	Bal.

2. Experimental procedure

In this study API 5L X80 pipeline steel plates of 100 × 400 × 15 mm were used and the chemical composition is shown in Table 1. The chemical analysis was carried out using arc spark optical emission spectrometer. However, C and S were tested separately with a dedicated fusion-combustion analyzer. This steel was produced by controlled thermomechanical processing and accelerated cooling (TMCP + ACC) [7]. Friction stir processing was performed in a dedicated TTI machine. Details on welding and processing parameter selection can be found elsewhere [5,6]. A single-processing pass, as also used at [15], was performed using a downward force control of 34 kN, spindle speed of 300 rev min^{-1}, transverse speed of 100 mm min^{-1} and average torque of 115 N m. A PCBN-WRe tool with 9.5 mm pin length was used.

Cylindrical samples with a reduced section diameter of 5 mm and free span of 5 mm were machined perpendicular to the rolling direction to perform physical simulations in a Gleeble® 3800 thermomechanical simulator. The thermal cycle was controlled by resistive heating, using a k-type thermocouple. The volumetric phase transformations were measured with a contact dilatometer. Quasi-static dilatometry tests were conducted at heating and cooling rates of 0.16 °C s^{-1} to stablish the near equilibrium phase transformation temperatures A_{c1} and A_{c3} on heating, and the A_{r3} and A_{r1} on cooling. Continuous cooling transformation (CCT) tests were conducted in slow (0.5, 1 °C s^{-1}), intermediated (3, 5, 10 and 20 °C s^{-1}) and rapid (40, 100, 140 and 170 °C s^{-1}) cooling rates. Time temperature transformation (TTT) experiments were performed to produce specific microstructures, such as isothermal perlite and bainite [16]. A fast cooling rate of 170 °C s^{-1} was used to perform the isothermal transformation cycles. The corresponding soaking times and transformation temperatures were 10,800 s at 700 °C, 9000 s at 650 °C, 3600 s at 600 °C, and 9000 s at 550, 500, 400 and 300 °C. Before cooling, both TTT and CCT cycles were austenitized at 950 °C during 900 s using a heating rate of 10 °C s^{-1}.

Microstructural characterization was performed in polished samples down to 0.05 μm colloidal silica and etched with Nital 3% to reveal the grain for LOM and SEM characterization. Micro-hardness measures were performed with load, dwell time and distance between indentations of 200 g, 13 s and 200 μm, respectively.

3. Results

3.1. *Friction stir processing microstructures*

The different microstructures found in the cross-section of the FSP sample are shown in Fig. 1. Additionally, Fig. 2 shows the hardness variations along the detail A–A schematized in

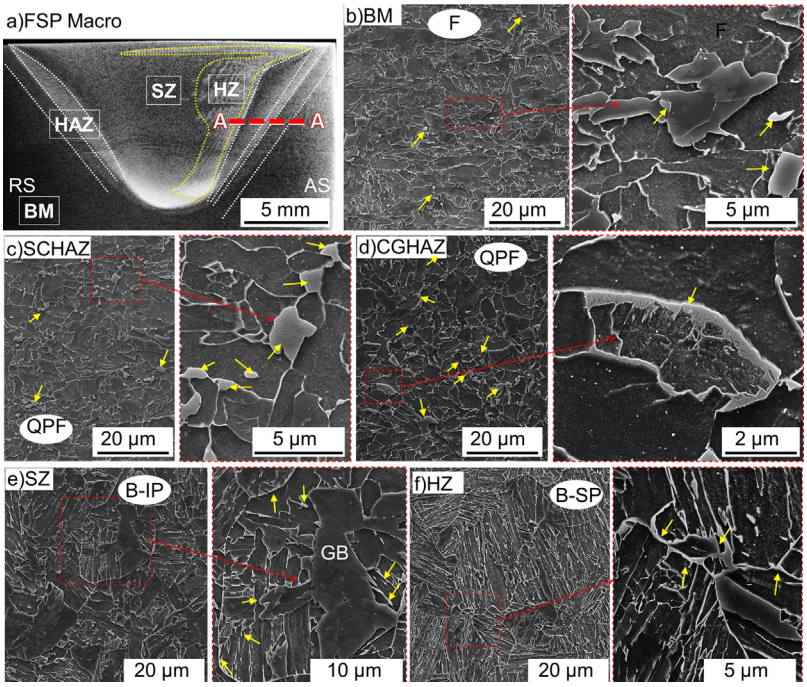

Fig. 1 – FSW microstructure zones: base metal (BM), heat-affected zone (HAZ), subcritical-grained HAZ (SCHAZ), coarse-grained HAZ (CGHAZ), stir zone (SZ) and hard zone (HZ). Microstructures: bainite packets with straight ferrite plates (B-SP), bainite packets with irregular ferrite plates (B-IP), granular bainite (GB), acicular ferrite (AF), quasi-polygonal ferrite (QPF), ferrite (F). Yellow arrows indicate position of some SP. SEM images, etched with Nital 3%.

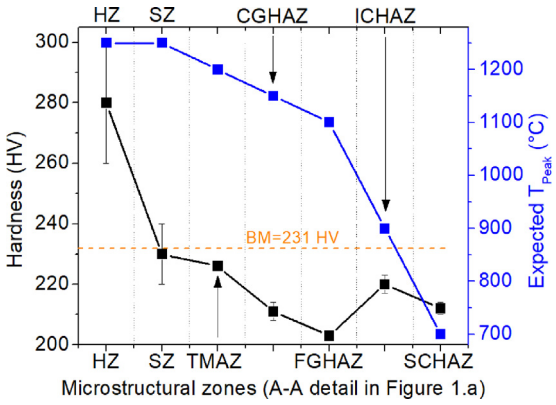

Fig. 2 – Measured hardness vs expected peak temperatures (T_{Peak}) [1]. Microstructural zones: stir zone (SZ), hard zone (HZ), thermo-mechanically affected zone (TMAZ), coarse-grained HAZ (CGHAZ), fine-grained HAZ (FGHAZ), inter-critical HAZ (ICHAZ), sub-critical HAZ (SCHAZ) and base metal (BM).

Fig. 1a, compared to the expected peak temperature (T_{Peak}), as suggested by Lienert et al. [1]. The starting microstructure (BM), was composed primarily by pancake-shaped ferrite (F) grains (Fig. 1b), bainite (B) and finely dispersed SP, mainly related to the MA constituent [8] (indicated by yellow arrows). Such SP are typically found at triple junctions and are characterized by blocky shapes. Regardless of the hardness reduction at the SCHAZ, neither changes in grain size nor in grain shape were observed when compared to the BM (Fig. 1b and c). The ICHAZ underwent partial austenitic transformation, while the FGHAZ and CGHAZ were fully austenitized during FSP. The ICHAZ, FGHAZ and CGHAZ evidenced slight softening when compared to the BM. In these cases, quasi-polygonal ferrite (QPF) was observed as the main microstructure (Fig. 1d). The SZ microstructure was composed by acicular ferrite (AF) [17], granular bainite (GB) [17,18] and coarse bainite packets with ferrite plates and irregular morphologies (B-IP) (Fig. 1e). Moreover, the HZ within the SZ presented coarse bainite packets with straight ferrite plates (B-SP) (Fig. 1f) [5].

The thermal cycles underwent at the CGHAZ, FGHAZ, ICHAZ and SCHAZ produced softer microstructures, when compared to 231 ± 2 HV at the BM, whereas the thermal cycles at the SZ and TMAZ regions resulted in little hardness modifications. The SCHAZ did not undergo noticeable microstructural changes. However, the peak temperature was high enough to cause tempering [19], reducing hardness when compared to the BM. The softening in HSLA steel depends on several factors, such as chemical composition, plate fabrication process, heat input and cooling rates [3]. Slow cooling rates (800–500 °C), which are associated to high heat inputs, provide large softening [20]. However, FSW/P provides little HAZ softening [3,6] when compared to arc welding [20].

3.2. *Physical simulation*

3.2.1. *Continuous cooling transformation tests*

The continuous cooling transformation (CCT) diagram, along with the resultant hardness and with some representative microstructures are presented in Fig. 3. The variation of the

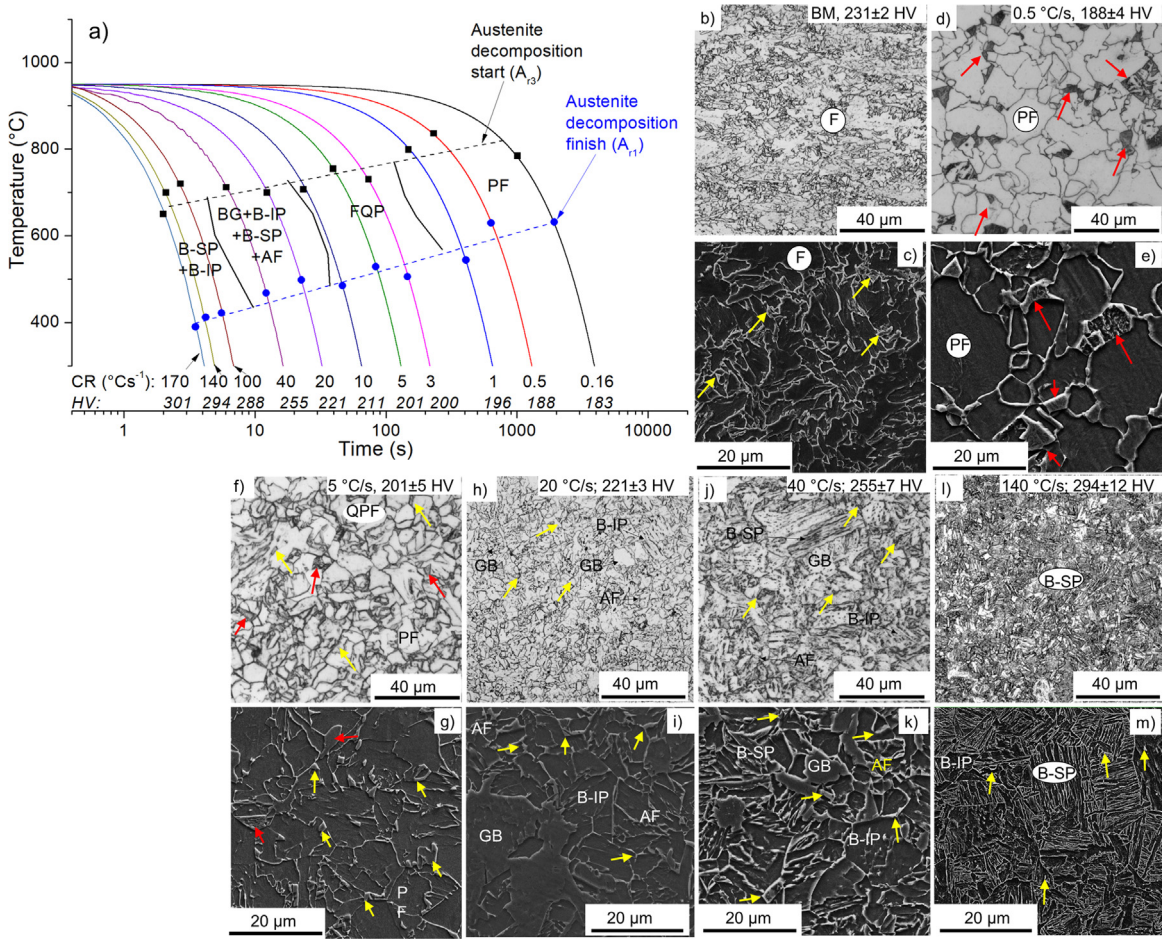

Fig. 3 – (a) Continuous cooling transformation (CCT) diagram showing the variation of the A_{r3} and A_{r1} transformation temperatures as a function of the cooling rate (CR). The resultant Vickers hardness is reported after each cooling cycle. The corresponding microstructural characterization is presented for: BM (b, c); and after cooling rates of 0.5 (d, e); 5 (f, g); 20 (h, i); 40 (j, k) and 140 °C s^{-1} (l, m). Microstructures: bainite packets with straight ferrite plates (B-SP), bainite packets with irregular ferrite plates (B-IP), granular bainite (GB), acicular ferrite (AF), polygonal ferrite (PF), quasi-polygonal ferrite (QPF), ferrite (F). Etched with Nital 3%. Red arrows: pearlite islands; yellow arrows: fine acicular secondary phases. (b, d, f, h, j, l) optical images and (c, e, g, i, k, m) SEM images.

A_{r3} (black squares) and A_{r1} (blue circles) temperatures with the cooling rate were plotted as a, depicted in Fig. 3a. Both A_{r3} and A_{r1} showed a decreasing tendency for faster cooling rates. Fig. 3b–m shows the resulting microstructures obtained after the most relevant cooling rates from the CCT diagram. Cooling rates between 0.16 °C s^{-1} and 1 °C s^{-1} resulted in microstructures composed mostly by PF and pearlite islands (P), indicated with red arrows. The resultant hardness values were between 183 ± 2 and 196 ± 3 HV. Between 3 and 20 °C s^{-1}, bainitic transformation along with two types of ferrite (PF and QPF) were observed. Less pearlite islands and the presence of fine acicular SP, indicated with yellow arrows, were also observed. This caused a relative hardness to increase from 200 ± 3 to 221 ± 3 HV. Nevertheless, cooling rates above 20 °C s^{-1} resulted mostly in QPF with elongated shapes, which difficulted the grain size determination. The samples cooled at 40 °C s^{-1} showed acicular ferrite (AF), granular bainite (GB), bainite with irregular (B-IP) and straight (B-SP) ferrite plates, and finely dispersed SP, resulting in a hardness increase to 255 ± 6 HV. The fastest cooling rates, between 100 and 170 °C s^{-1}, resulted manly in bainite with straight ferritic plates (B-SP), which provided the hardest microstructures, between 288 ± 6 and 301 ± 5 HV.

Fig. 4 shows the dilatometric heating and cooling curves as a function of temperature for the CCT cycles. The variation of ferrite to austenite transformation start (A_{c1}) and finish (A_{c3}) temperatures during heating, as well as the austenite decomposition start (A_{r3}) and finish (A_{r1}) temperatures during cooling are indicated by red arrows. During the quasi-static dilatometry test conducted at 0.16 °C s^{-1} (Fig. 4a), the A_{c1} and A_{c3} were found at 680 and 915 °C, respectively. During cooling, A_{r3} was found at 785 °C and A_{r1} at 630 °C. Considering the BM microstructure as the starting zero dilatation state, a residual contractive condition with a dimensional change of about –36 µm was obtained after cooling down to room temperature.

The complete austenitization and slow cooling rate provided a stress relaxation of the ferritic matrix formerly submitted to hot rolling and accelerated cooling. A new matrix with the presence of PF with presence of finely dispersed P and

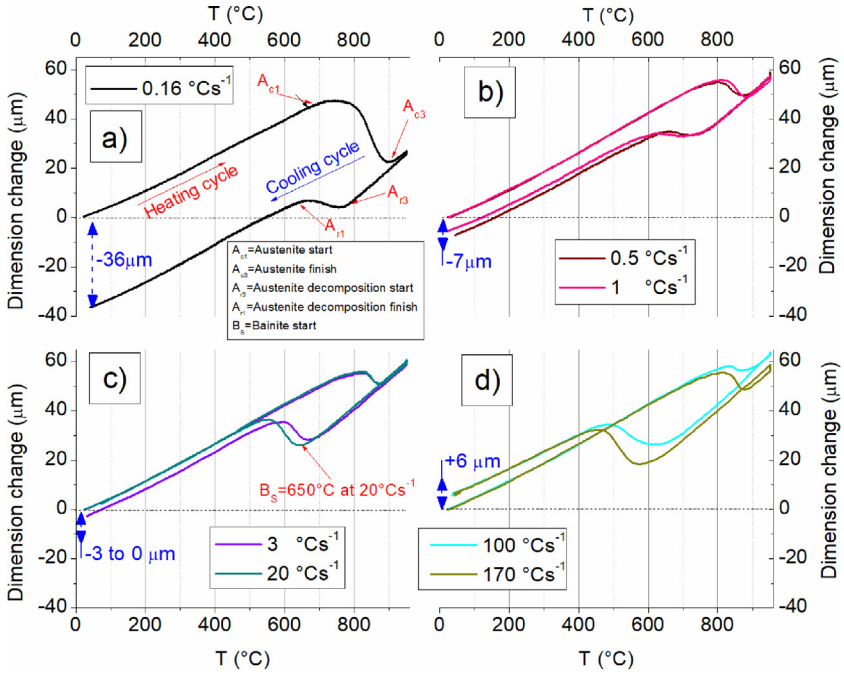

Fig. 4 – Dilatometric heating and cooling curves showing the variation of A_{c1}, A_{c3}, A_{r3} and A_{r1} transformation temperatures as a function of the cooling rate; (a) dilatometry test in quasi-static rates, (b) slow cooling rates, (c) intermediated cooling rates and (d) fast cooling rates.

SP was obtained. By increasing the cooling rates, the resultant contractive condition, i.e., relaxation was progressively reduced, as can be seen for the slow and intermediated cooling rates in Fig. 4b and c, respectively. A size reduction of the ferritic grains was observed, accompanied by a transition from polygonal to quasi-polygonal (QPF) shape. Faster cooling rates, (above 20 °C s^{-1}) started showing even positive or residual expansive conditions, which are associated to displacive transformations [21], such as bainite and martensite. However, as evidenced in Fig. 3h–m, the microstructures were composed mainly by mixtures of bainite with different morphologies. The formation of acicular ferrite and the transition from GB to B-SP were observed when the cooling rate was severely increased. No discernible martensitic transformation was evidenced due to the absence of an additional volumetric expansion below 400 °C. Therefore, it is expected that even after cooling rates as severe as 170 °C, the microstructure will be composed mainly by B-SP with little or no martensite.

3.2.2. *Time temperature transformation experiments*

Fig. 5 shows the summary of the phase transformations and resulting microstructures after fast cooling and isothermal transformations. The dilatation curves for the isothermal cycles as a function of temperature are shown in Fig. 5a and b. Additional dilatometric information regarding the isothermal stage is shown in Fig. 5c, as a function of time.

The isothermal expansion and the absence of any further dilatation upon cooling evidenced the complete isothermal formation of pearlite for the high temperature isothermal cycle of 700 °C. As shown in Fig. 5c, the austenite is completely exhausted within the first 1500 s of isothermal transformation. The microstructures in (d, e) evidenced mostly PF and QPF with grain diameters of 10 ± 0.6 μm, along with the presence of pearlite islands (red arrows), with a resultant hardness of 169 ± 9 HV. The isothermal transformations between 700 and 550 °C (d, i) reduced the amount and size of the pearlitic islands (8 ± 1 μm to 3 ± 1 μm), as well grain refinement of the PF and QPF from 10 ± 0.6 μm to 6 ± 0.4 μm. The hardness values increased 193 ± 7 HV and 219 ± 3 HV, respectively. As indicated in Fig. 5b, an evident change in slope upon cooling below 600 °C indicated the initial stage of the bainitic transformation. This is due to the delayed austenite decomposition caused by the fast cooling rate of 170 °C, which displaced the A_{r3} temperature to around 650 °C (Fig. 4d). The bainite start temperature (B_S) was calculated using Eq. (1) [22] for the nominal. The calculated value of 622 °C was in good agreement with the experimental observations in Fig. 5a and b.

On the other hand, the low temperature isothermal treatments between 500 and 300 °C (j–o) showed a clear transition from PF + QPF, to GB + AF + B(IP) + B(SP). For these cases, the formation of pearlite was suppressed, favoring the isothermal bainitic transformation. The grain diameters for the isothermal treatments below 600 °C could not be reliably measured due to the resulting irregular and elongated shapes. However, hardness increased from 244 ± 4 up to 289 ± 7 HV as the isothermal temperature decreased from 500 to 300 °C, respectively, due to the formation of such acicular products. Only partial isothermal bainitic transformation occurred for the cycles between 550 and 500 °C, since the bainitic transformation already started upon cooling below 650 °C. According to Fig. 5c, a slight bainitic expansion occurred right after the starting of the isothermal stage at 550 and 500 °C. The latter presents a smaller overall expansion due to the almost complete transformation before reaching the isothermal stage.

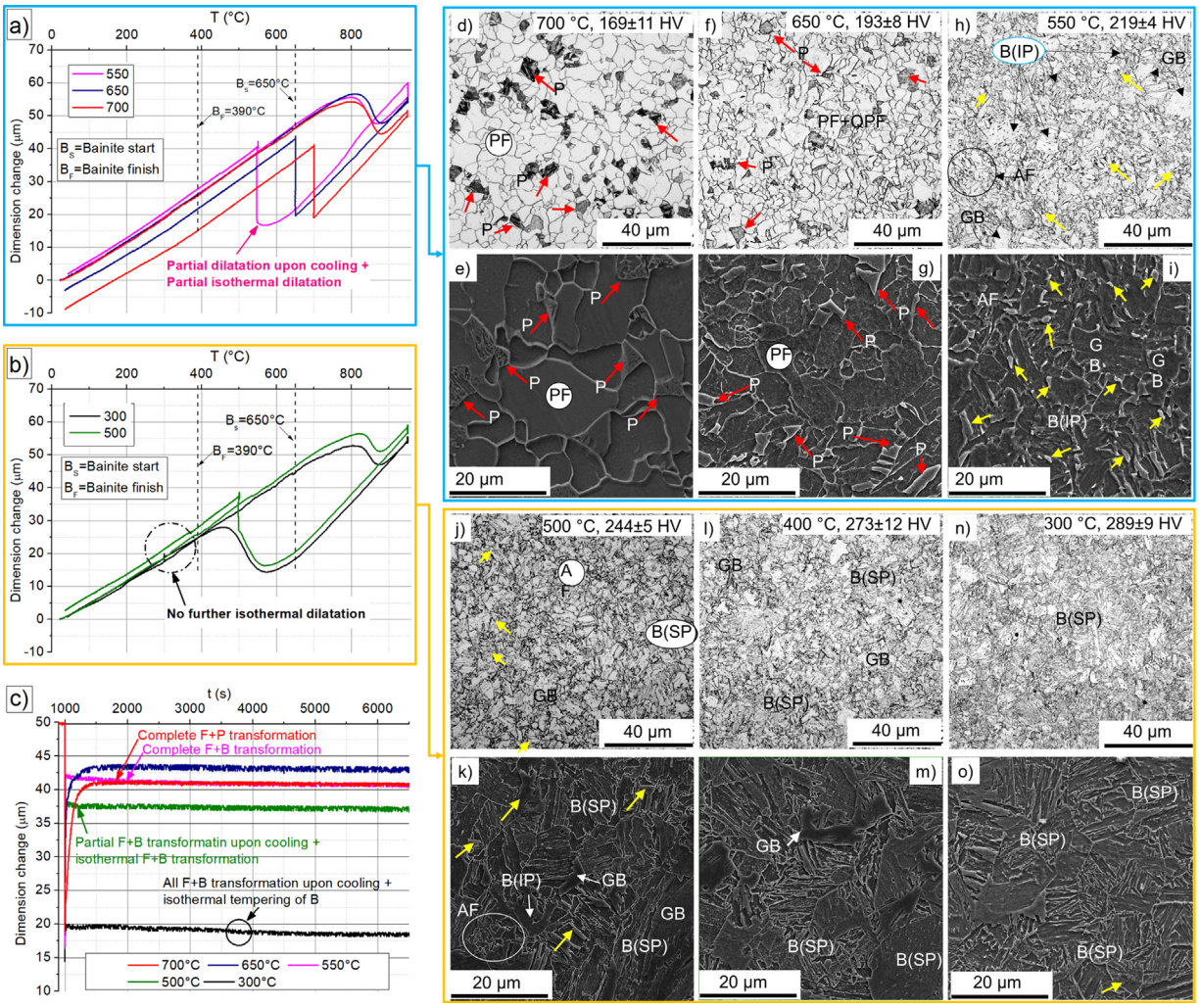

Fig. 5 – Dilatometric results during the physical simulation of the time temperature transformation cycles, involving rapid cooling at 170 °C s^{-1} and isothermal transformations at: (a) 700 °C during 10,800 s, 650 °C during 9000 s and 550 °C during 9000 s; (b) 500 °C during 9000 s and 300 °C during 9000 s. (c) Dimensional change associated to the isothermal stages. F: ferrite; B: bainite. The corresponding microstructures after isothermal transformations are presented: 700 °C/10,800 s (d, e); 650 °C/9000 s (f, g); 550 °C/9000 s (h, i); 500 °C/9000 s (j, k); 400 °C/9000 s (l, m); and 300 °C/9000 s (n, o). Microstructures: second phases (SP), polygonal ferrite (PF), quasi-polygonal ferrite (QPF), granular bainite (GB), bainite packets with straight ferrite plates (B-SP), bainite packets with irregular ferrite plates (B-IP) and acicular ferrite (AF). Etched with Nital 3%. Red arrows: pearlite islands; yellow arrows: fine acicular secondary phases. (d, f, h, j, l, n) optical images and (e, g, i, k, m, o) SEM images.

Therefore, no isothermal transformation occurred at 300 °C (black arrow in Fig. 5b) as the bainitic end temperature was detected around 390 °C. The steady slope reduction within the first 5000 s, evidenced in Fig. 5c, was most likely caused by the auto-tempering of the bainitic microstructure. This effect is more evident when directly comparing the microstructures in Fig. 6a and b (fast cooling at 170 °C s^{-1}), to the ones in Fig. 6c and d (fast cooling at 170 °C s^{-1} and isothermal transformation at 300 °C during 9000 s). A degeneration of the B-SP toward more irregular bainitic plates was clearly observed for the second case. Furthermore, it is interesting to notice that no martensitic transformation was observed upon cooling for neither of the compared conditions. The martensitic start temperature (M_S) was calculated using Eq. (2) [23] based on the nominal composition and the measured A_{r3} temperature. Although the martensitic transformation is expected to occur at 194 °C, this was not observed experimentally. Therefore, cooling rates faster than 170 °C s^{-1} will be needed to form martensite in this X80 pipeline steel.

$$B_s(^\circ C) = 745 - 110C - 59Mn - 39Ni - 68Cr - 106Mo + 17MnNi + 6Cr^2 + 29Mo^2 \quad (1)$$

$$M_s(K) = A_{r3} - 199.8(C + 1.4N) - 17.9Ni - 21.7Mn - 6.8Cr - 45.0Si - 55.9Mo - 1.9(C + 1.4N)(Mo + Cr + Mn) - 14.4[(Ni + Mn)(Cr + Mo + Al + Si)]^{1/2} - 410 \quad (2)$$

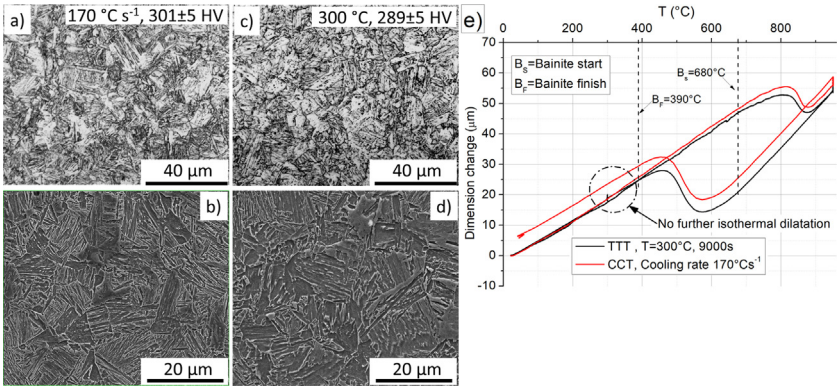

Fig. 6 – Microstructural results after: CCT with a fast cooling rate of 170 °C s^{-1} (a, b); and after auto-tempering of bainite after a fast cooling of 170 °C s^{-1} and subsequent isothermal stage at 300 °C during 9000 s (c, d). The relative dimension change, as a function of time, is shown in (e). SEM and LOM observed samples were etched with Nital 3%.

4. Discussion

Fig. 7 shows the summarized microstructural and hardness results as a function of the thermal cycle. The resultant microstructures were divided in four blocks: Predominantly PF + P (yellow), QPF + PF (cyan), GB + BIP + BSP + AF (magenta) and GB + BP (gray). A correlation between the microstructures and the cooling rates for the CCT and TTT cycles was observed. Slow cooling rates from 0.16 to 1 °C s^{-1} during CCT cycles were equivalent to fast cooling followed by isothermal transformation between 700 and 650 °C during 10,800 s and 9000 s, respectively, favoring the formation of PF + P. Formation of QPF + PF was beneficiated by increasing the cooling rate from 3 to 20 °C s^{-1} for the CCT cycles, or by using fast cooling and isothermal transformation between 600 and 650 °C during 3600 and 9000 s, respectively. Bainitic microstructures, GB + B-IP + B-SP and AF, were observed for cooling rates faster than 20 °C s^{-1}. The morphology of the bainite packets and their ferrite plates became straighter and more elongated for cooling rates faster than or equal to 40 °C s^{-1}. In addition, GB and B-IP were observed after isothermal transformation at 550 and 500 °C during 9000 s each. Although bainitic microstructures were also observed for the fast cooling and isothermal cycles below 500 °C, a difference in morphology and hardness could be observed.

The bainitic transformation started upon cooling below 650 °C and ended around 390 °C. Therefore, the isothermal stages below 400 °C resulted in auto-tempering of the microstructure, changing the B-SP into more irregular or degenerated bainitic plates. The auto-tempering effect is the reason for the lower hardness of 289 ± 5 HV (after fast cooling

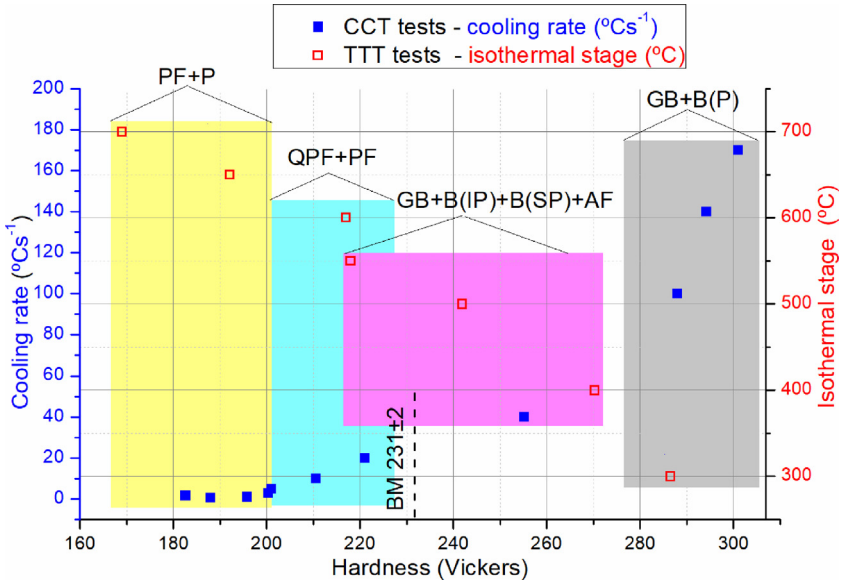

Fig. 7 – Microstructures and hardness evolution as a function of the thermal cycle. Microstructures: polygonal ferrite (PF), pearlite (P), quasi-polygonal ferrite (QPF), granular bainite (GB), bainite packets with straight ferrite plates (B-SP), bainite packets with irregular ferrite plates (B-IP) and acicular ferrite (AF).

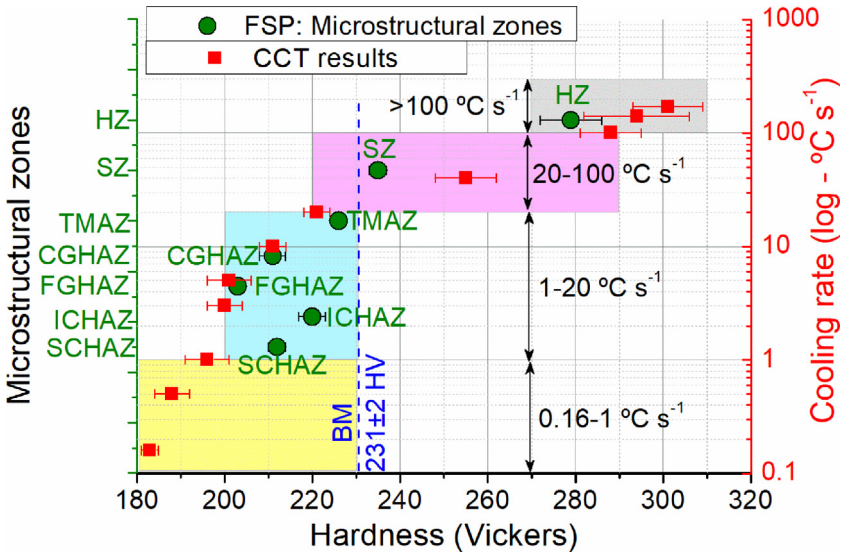

Fig. 8 – Hardness distribution of the microstructural zones of the FSP plate and samples submitted to physical simulations. Microstructures zones: stir zone (SZ), thermo-mechanically affected zone (TMAZ), coarse-grained HAZ (CGHAZ), fine-grained HAZ (FGHAZ), inter-critical HAZ (IGHAZ), sub-critical HAZ (SCHAZ) and base material (BM).

and isothermal transformation at 300 °C), when compared to 301 ± 5 HV (obtained after continuous cooling at 170 °C s^{-1} down to room temperature). During low temperature tempering of bainite in HSLA steels, a ferritic matrix with small cementite (~5 nm) and Cr and Mn-rich cementite has been reported [24]. Hence, the bainitic matrix loses carbon, causing a volumetric contraction and a hardness reduction.

Fig. 8 shows a brief comparison in terms of microstructural zones, cooling rates and harnesses between the FSP and physical simulation results. The cooling rates below 1 °C s^{-1} were not representative for any of the FSP microstructural zones due to the massive pearlitic transformation. The PF + P microstructure resulted in a noticeable hardness drop below 200 HV. Besides, none of the TMAZ, CGHAZ, FGHAZ and IGHAZ zones evidenced the presence of pearlitic islands. Even though these four HAZs experienced partial or total austenitization, the fast heating rate inherent to FSP prevented the pearlitic transformation to occur. Besides, the FSP thermal cycle at the SCHAZ is only expected to degenerate the microstructure toward the production of ferrite and carbides, similar to an auto-tempering effect. However, this was not experimentally observed due to the short exposure of this zone to the FSP thermal cycle.

Cooling rates below 20 °C s^{-1} presented similar microstructural features (QF, QPF and blocky SP) and hardness (200–230 HV) when compared to TMAZ, CGHAZ, FGHAZ and IGHAZ zones after FSP. This softening effect, which depends on chemical composition, plate fabrication process, heat input and cooling rates [3,15] has been reported in the HAZ of HSLA steel processed by FSW/P [3,6] and arc welding [20]. Cooling rates between 20 and 40 °C s^{-1} resulted in similar microstructures (AF + GB + B-IP + B-SP), when compared to the SZ. The average SZ hardness of 235 ± 15 HV was contained in the hardness range of 220–250 HV, obtained for cooling rates between 20 and 40 °C s^{-1} [15].

Furthermore, the hard zone inside the SZ showed the highest hardness of 300 HV, and its microstructure was composed mainly by B-SP. This condition was comparable to the B-SP + GB microstructure, found after cooling rates faster than 40 °C s^{-1}. The hardness values for the cooling rates between 100 and 140 °C s^{-1} matched those at the HZ. This suggest that the HZ locally experienced higher peak temperatures, and, consequently higher cooling rates when compared to the SZ. This is consistent with computational simulation results available in literature [1,15,25]. On the other hand, Allred et al. [11] performed several heat treatments by means of physical simulation for an API 5L X65 steel. It was proposed that the cooling rate was the dominant factor for the different hardness values found at the SZ and HZ, reporting cooling rates between 20 °C s^{-1} and 240 °C s^{-1} within SZ and HZ [11]. In addition, Nelson et al. [12] suppressed the HZ, forcing cooling rates below 20 °C s^{-1} by using different materials as backing plates to control the heat extraction during FSW.

Regarding arc-welding, the main factor affecting the grain size of the HAZ is the peak temperature, where high peak temperatures present slow cooling rates allowing austenite grain coarsening [20], which aids hardening of the as-welded microstructure. At the present study, the grain size of the coarse-grained microstructure was equivalent to that from the BM. In addition, the distribution of the secondary phases did not show a necklace-like arrange, which is considered to be the cause of brittle fracture at HAZ of arc welding [26]. As a consequence, good impact toughness results were found [5].

An approach to improve toughness can be the reduction of the overall cooling rate, so as to obtain a more homogenous hardness distribution, as performed by [12]. From the present study, it can be observed that reducing cooling rates below 100 °C s^{-1} will avoid the HZ-like microstructures, which yields to toughness enhancements [12]. However, specifically controlling the cooling rates between 20 and 40 °C s^{-1} is expected

to offer tough microstructures, such as QPF, AF and B-IP. Finally, controlling the cooling rate below 20 °C s^{-1} might lead to excessive softening of the weld, by the formation of PF and QPF with presence of pearlite.

5. Conclusions

A series of CCT and TTT experiments were conducted through physical simulation in order to produce and isolate specific microstructures in a controlled way. The results were useful to understand the mixed and complex microstructures produced by the thermal cycle of FSP. The main conclusions are:

- Physical simulations performed for slow cooling rates between 0.5 and 1 °C s^{-1} showed primarily a soft matrix composed by polygonal ferrite and pearlite. The microstructure obtained for cooling rates below 5 °C s^{-1} was not representative to any of the microstructural zones obtained after FSP. Nevertheless, the hardness values at the SCHAZ, ICHAZ were similar to cooling rates between 1 and 3 °C s^{-1}.
- Intermediated cooling rates between 3 and 20 °C s^{-1} presented microstructures with polygonal and quasi-polygonal ferrite with little or no pearlite, along with finely dispersed acicular secondary phases. The hardness values and microstructures at the FGHAZ and CGHAZ were obtained for cooling rates between 4 and 10 °C s^{-1}.
- Rapid cooling rates between 20 and 40 °C s^{-1} evidenced the preferential formation of acicular ferrite, granular bainite and bainite with irregular ferrite plates. Above 40 °C s^{-1}, the granular bainite decreased and the bainite with straight ferrite plates was dominant. The microstructure and hardness at the SZ was best represented for cooling rates between 20 and 40 °C s^{-1}. Whereas, the HZ was in best agreement with the cooling rate of 100 °C s^{-1}.
- For cooling rates above 20 °C s^{-1}, the bainitic transformation was preferred over the pearlitic transformation. The bainitic transformation started at 650 °C and finished at 390 °C upon continuous cooling. As no pearlitic islands were observed along the SZ, it can be assumed that the cooling rates at such microstructural zone are above 20 °C s^{-1}.
- After physical simulations of both CCT and TTT cycles, evidence of martensitic formation was found neither by dilatometry nor by microstructural examination. Therefore, the martensitic formation during FSP of this steel is not expected to be representative if the cooling rates at the weld are at or below 170 °C s^{-1}.
- Controlling the cooling rate to be around 20 and 40 °C s^{-1} is expected to produce microstructure and hardness values similar to the base metal condition, relative to a thermo-mechanical controlled processes followed by accelerated cooling.

Conflicts of interest

The authors declare no conflicts of interest.

Acknowledgements

We would like to thank to the Brazilian Nanotechnology National Laboratory (LNNano) for the use of the FEI ® Quanta 650FEG SEM, FSW machine, Gleeble® 3800 thermomechanical simulator and metallography facilities; PETROBRAS for providing economic funding; Tenaris Confab for the material donation and Mr. Joel Alencar for his collaborations with the metallography technical assistant.

REFERENCES

[1] Lienert TJ, Stellwag WL, Grimmett BB, Warke RW. Friction stir welding studies on mild steel – process results, microstructures, and mechanical properties are reported. Weld J Suppl 2003:1–9.
[2] Fairchild DP, Bangaru NV, Koo JY, Harrison PL, Ozekcin A. A study concerning intercritical HAZ microstructure and toughness in HSLA steels. Weld J 1991;70:321s–30s.
[3] Ozekcin A, Jin HW, Koo JYN, Bangaru V, Ayer R, Vaughn G, et al. A microstructural study of friction stir welded joints of carbon steels. In: Fourteenth international offshore polar engineering conference, vol. 14. 2004. p. 284–8.
[4] Cho H-H, Kang SH, Kim S-H, Oh KH, Kim HJ, Chang W-S, et al. Microstructural evolution in friction stir welding of high-strength linepipe steel. Mater Des 2012;34:258–67, http://dx.doi.org/10.1016/j.matdes.2011.08.010.
[5] Avila JA, Lucon E, Sowards J, Mei PR, Ramirez AJ. Assessment of ductile-to-brittle transition behavior of localized microstructural regions in a friction-stir welded X80 pipeline steel with miniaturized charpy V-notch testing. Metall Mater Trans A 2016;47:2855–65, http://dx.doi.org/10.1007/s11661-016-3473-z.
[6] Avila JA, Rodriguez J, Mei PR, Ramirez AJ. Microstructure and fracture toughness of multipass friction stir welded joints of API-5L-X80 steel plates. Mater Sci Eng A 2016;673:257–65, http://dx.doi.org/10.1016/j.msea.2016.07.045.
[7] Nishioka K, Ichikawa K. Progress in thermomechanical control of steel plates and their commercialization. Sci Technol Adv Mater 2012;13:023001, http://dx.doi.org/10.1088/1468-6996/13/2/023001.
[8] Zajac S, Schwinn V, Tacke KH. Characterisation and quantification of complex bainitic microstructures in high and ultra-high strength linepipe steels. Mater Sci Forum 2005;500–501:387–94, http://dx.doi.org/10.4028/www.scientific.net/MSF.500-501.387.
[9] Dmitrieva O, Ponge D, Inden G, Millán J, Choi P, Sietsma J, et al. Chemical gradients across phase boundaries between martensite and austenite in steel studied by atom probe tomography and simulation. Acta Mater 2011;59:364–74, http://dx.doi.org/10.1016/j.actamat.2010.09.042.
[10] Hermenegildo TF, Santos TF, Torres EA, Afonso CRM, Ramirez AJ. Microstructural evolution of HSLA ISO 3183 X80M (API 5L X80) friction stir welded joints. Met Mater Int 2018, http://dx.doi.org/10.1007/s12540-018-0111-x.
[11] Allred J. An investigation into the mechanisms of formation of the hard zone in FSW X65. Brigham Young University; 2013.
[12] Nelson TW, Rose S. Controlling hard zone formation in friction stir processed HSLA steel. J Mater Process Technol 2016;231:66–74, http://dx.doi.org/10.1016/j.jmatprotec.2015.12.013.

[13] Wei L, Nelson TW. Influence of heat input on post weld microstructure and mechanical properties of friction stir welded HSLA-65 steel. Mater Sci Eng A 2012;556:51–9.
[14] Aydin H, Nelson TW. Microstructure and mechanical properties of hard zone in friction stir welded X80 pipeline steel relative to different heat input. Mater Sci Eng A 2013;586:313–22, http://dx.doi.org/10.1016/j.msea.2013.07.090.
[15] Avila JA, Giorjao RAR, Rodriguez J, Fonseca EB, Ramirez AJ. Modeling of thermal cycles and microstructural analysis of pipeline steels processed by friction stir processing. Int J Adv Manuf Technol 2018;98:2611–8, http://dx.doi.org/10.1007/s00170-018-2408-9.
[16] Bhadeshia HKDH, Christian JW. Bainite in steels. Metall Trans A 1990;21:767–97, http://dx.doi.org/10.1007/BF02656561.
[17] Kyung Sung H, Ho Lee D, Yong Shin S, Lee S, Yong Yoo J, Hwang B. Effect of finish cooling temperature on microstructure and mechanical properties of high-strength bainitic steels containing Cr, Mo, and B. Mater Sci Eng A 2015;624:14–22, http://dx.doi.org/10.1016/j.msea.2014.11.035.
[18] Kang JS, Seol JB, Park CG. Three-dimensional characterization of bainitic microstructures in low-carbon high-strength low-alloy steel studied by electron backscatter diffraction. Mater Charact 2013;79:110–21, http://dx.doi.org/10.1016/j.matchar.2013.02.009.
[19] Krauss G. Steels: processing structure and perfomance. 1st ed. ASM International; 2005.
[20] Maurer W, Ernst W, Rauch R, Vallant R, Enzinger N. Evaluation of the factors influencing the strength of HSLA steel weld joint with softened HAZ. Weld World 2015;5:1–14, http://dx.doi.org/10.1007/s40194-015-0262-z.
[21] Escobar JD, Faria G, Wu L, Oliveira JP, Mei PR, Ramirez AJ. Austenite reversion kinetics and stability during tempering of a Ti-stabilized supermartensitic stainless steel: correlative in situ synchrotron X-ray diffraction and dilatometry. Acta Mater 2017;138:92–9, http://dx.doi.org/10.1016/j.actamat.2017.07.036.
[22] Lee Y. Empirical formula of isothermal bainite start temperature of steels. J Mater Sci Lett 2002;21:1253–5.
[23] Dai QX, Cheng XN, Zhao YT, Luo XM, Yuan ZZ. Design of martensite transformation temperature by calculation for austenitic steels. Mater Charact 2004;52:349–54, http://dx.doi.org/10.1016/j.matchar.2004.06.008.
[24] Peet MJ, Babu SS, Miller MK, Bhadeshia HKDH. Tempering of low-temperature bainite. Metall Mater Trans A 2017;48:3410–8, http://dx.doi.org/10.1007/s11661-017-4086-x.
[25] De A, Bhadeshia HKDH, DebRoy T. Friction stir welding of mild steel: tool durability and steel microstructure. Mater Sci Technol 2014;30:1050–6, http://dx.doi.org/10.1179/1743284714Y.0000000534.
[26] Li X, Ma X, Subramanian SV, Shang C. EBSD characterization of secondary microcracks in the heat affected zone of a X100 pipeline steel weld joint. Int J Fract 2015;193:131–9, http://dx.doi.org/10.1007/s10704-015-0024-3.